The Lensing Cluster MS0440+0204 Seen by HST, ROSAT and ASCA: I. Cluster Properties[1]

I. M. Gioia[2,3,4], E. J. Shaya[5], O. Le Fèvre [6], E.E. Falco[7], G.A. Luppino[2,4] and F. Hammer[6]

arXiv:astro-ph/9712004v1 30 Nov 1997

ABSTRACT

We present an analysis of the properties of the lensing cluster MS0440+0204 at z=0.1965. MS0440+0204 has been observed with a variety of telescopes at diverse wavelengths: from the ground with *CFHT, MMT* and *KECK* and from Earth orbit with *HST, ROSAT* and *ASCA*. Mass determinations are separately obtained from galaxy virial motions and X-ray profile fitting. A simple β-model fit to the X-ray data yields a mass of $(1.3\pm0.2) \times 10^{14} M_\odot$ within 583 kpc of the cluster center, but more general models fit all of our data better and allow a wider range of masses that are consistent with the lensing data. In addition, the X-ray data yield a mass distribution profile that is well described by a β model with a core radius of 26.7 kpc. The velocity dispersion of galaxies yields a mass of $4.8^{+1.5}_{-0.94} \times 10^{14} M_\odot$ within 900 kpc. In the inner 24″.5 there are 24 arcs that appear to be strong gravitationally lensed images of background sources. Models of the cluster mass distribution and its lensing properties reveal 5 background sources at various redshifts each forming 2 or more arcs. We do not have a redshift for any arc with multiple images, therefore we can only place upper and lower limits to the mass of the cluster from gravitational lensing. At 100 kpc, the lower limit mass from lensing is about a factor of 2 greater than the X-ray determined mass. The rate of increase in the projected mass at this radius also is greater for the

---

[2]Institute for Astronomy, 2680 Woodlawn Drive, Honolulu, HI 96822

[3]Istituto di Radioastronomia del CNR, Via Gobetti 101, I-40129, Bologna, ITALY

[4]Visiting Astronomer at CFHT, operated by the National Research Council of Canada, le Centre National de la Recherche Scientifique de France and the University of Hawai′i , and at the W. M. Keck Observatory, jointly operated by the California Institute of Technology and the University of California

[5]Physics Department, University of Maryland, College Park, MD 20742

[6]DAEC, Observatoire de Paris Meudon, 92195 Meudon Principal Cedex, FRANCE

[7]Center for Astrophysics, 60 Garden Street, Cambridge, MA 02138

lens model than the X-ray determination. To reconcile the mass estimates from the X-rays and the lensing and to try to understand the steep slope of the gravitational lens mass, we tentatively explore a model with a supercluster surrounding the cluster and with a mass profile that increases more rapidly than a β model at large radii.

Subject headings: galaxies: clusters - general - individual: MS0440+0204; cosmology: gravitational lensing - dark matter; X-rays: general

1. Introduction

As the largest gravitationally bound structures known, clusters can set clear constraints on the formation of structure and on the composition of the universe. Three independent techniques have been used to determine the mass distribution in galaxy clusters. The oldest and most conventional approach is based on galaxy velocity dispersion and application of the virial theorem. Here it is assumed that galaxy orbits are isotropic and that light traces the dark matter. A second method derives gravitational mass profiles from X-ray observations under the assumptions of thermal hydrostatic equilibrium and spherical symmetry. In this technique only two observables must be known to reconstruct the distribution of mass, the electron density of the cluster gas and its temperature, clearly an advantage with respect to the often limited optical data available to define the cluster structure. The X-ray derived mass, however, may not necessarily be representative of the true cluster mass if merger compression or shocks are present. Over the last ten years it has been possible to determine cluster masses using the effect of gravitational lensing, both in its strong and weak manifestations (see the excellent review of Fort and Mellier, 1994, for a list of clusters that has been analyzed.). The lensing method has the advantage that the mass measurement is independent of the thermodynamical state of the gravitating matter. The weak distortions (Tyson *et al.* 1990; Kaiser and Squires, 1993) are particularly suited to map cluster mass at large radii. Strong lensing is restricted to the cluster core.

The use of the three techniques in conjuction allows an examination of the uncertainties of each method and provides a unique possibility to study the dynamical and physical state of the gas and dark matter in clusters. It is worth noting that even if theoretically one should obtain the same masses if clusters are dynamically relaxed, in practice comparisons of masses derived from dynamical analyses and gravitational lensing have shown a significant discrepancy in the mass estimates ($M_{lens}/M_{dyn} \sim$ from 5 to 2 going from inner $250 - 300$ kpc of the cluster center up to 1 Mpc; see Wu and Fang, 1996, 1997 and references therein), but there are exceptions as mentioned below.

Several possibilities have been suggested to resolve this discrepancy. Among others: inadequacy of the isothermal, hydrostatic equilibrium models of the X-ray analyses that cause systematic underestimate of the cluster mass (Wu and Fang 1996); projection effect of an

asymmetrical matter distribution (Miralda-Escudé and Babul, 1995); presence of substructures in X-ray clusters and cluster mergers (Henry and Briel 1995, 1996; Markevitch 1996) which would help to explain the discrepancy in A2218 (Kenib *et al.* 1995; Squires *et al.* 1996a) and in A2219 (Smail *et al.* 1995a); inhomogeneous intracluster medium (Miralda-Escudé and Babul, 1995); the possibility of X-ray lensing (in A2218, Markevitch 1997); existence of nonthermal cosmic ray pressure which could support the intracluster ionised gas (Ensslin *et al.* 1997); offsets between X-ray and lensing centres and overestimate of the core radii of the dominant mass clumps in non-cooling flow systems (Allen, 1997). However, recent analyses with better data show a more complex picture that will lead to a better understanding of the physical processes going on in clusters.

Marginal agreement of the mass determinations from X-ray and lensing analyses is found in A2163 (Miralda-Escudé and Babul 1995), and confirmed by Squires *et al.* 1997, using weak lensing and new ROSAT HRI and PSPC data. A similar analysis by Smail *et al.* 1995b, for the Medium Survey clusters MS1455+22 and MS0016+16 found agreement between the lensing and X-ray masses. A consistent picture is constructed for A2390 by Pierre *et al.* 1996, and Squires *et al.* 1996b. Allen *et al.* 1996, present a multi-phase X-ray analysis of PKS0745−191, a regular and relaxed cluster with a massive cooling flow. The excellent agreement of the mass distributions lead them to conclude that the X-ray gas in PKS0745−191 is in hydrostatic equilibrium, and that non-thermal pressures components are not required by the data, differently from the cases of A1689 or A2218 (Miralda-Escudé and Babul, 1995; Loeb and Mao 1994). In a recent analysis of 13 clusters observed with ASCA and ROSAT, Allen points out that the X-ray and strong gravitational lensing mass measurements show excellent agreement for the cooling-flow clusters in his sample, while for the non-cooling flow clusters, the masses determined from the strong lensing data exceed the X-ray values by factors of 2−4. Allen suggests that these discrepancies can be reconciled if one takes into account that the dynamical activity observed in non-cooling flow clusters has caused the X-ray analyses to overestimate the core radii of the dominant mass clumps. Other factors as substructure and line-of-sight alignments of material towards the cluster cores may also contribute to the discrepancies. A quite different and interesting approach is taken by Smail *et al.* (1997) to analyze a small sample of 12 clusters observed by the Hubble Space Telescope (HST). From the comparison of the mean gravitational shear strength with the cluster X-ray luminosities they develop a model used to predict the relationship expected from properties of local clusters. In this way they can distinguish between models for the evolution of the cluster properties. It is an innovative and promising study to measure cluster evolution once an expanded and better defined sample of clusters are examined.

In this paper, we present a study of the gas and mass distributions of the cluster of galaxies MS0440+0204. Originally discovered through its X-ray emission in the Extended Medium Sensitivity Survey (EMSS; Gioia *et al.* 1990), MS0440+0204 was part of a Mauna Kea based observational program to search for arcs and arclets in a complete sample of X-ray luminous medium-distant (0.15≤z≤0.83) clusters of galaxies. At a redshift of z=0.1965, MS0440+0204 has

the most striking example of an arc system in a compact, centrally condensed cluster. Ground based CCD observations of MS0440+0204 show at least 15 blue segments of circular structures surrounding a multiple nucleus cD galaxy (Luppino *et al.* 1993). The arcs are unresolved even in superb observing conditions (seeing ∼0.5″) at Mauna Kea Observatory.

We have extended the study of MS0440+0204 with the refurbished HST and with X-ray satellite observations. Deep images, acquired with the WFPC2 camera aboard HST, reveal detailed structures in both the previously known arcs and the newly discovered arcs. Constraints on the mass of the cluster are derived from detailed modeling of these arcs. Additional mass estimates are obtained from X-ray observations of MS0440+0204 with ROSAT/HRI and ASCA. We also acquired spectra for 40 cluster members from the ground and, therefore, were able to estimate the velocity dispersion of the cluster, which yields an independent dynamical estimate of the cluster mass. We present both the optical and X-ray data that we have acquired and make comparisons between the diverse and complementary mass distribution estimates for MS0440+0204. To reconcile the discrepancy of mass estimates from the dynamical and lensing analyses, we present a very simple model with a mass profile that increases more rapidly than a β model at large radii. The model explored in this paper is one with two isothermal spheres. We remind here that more general models fit all of our data better and allow a wider range of masses that are consistent with the lensing data (Shaya *et al.* 1998). We emphasize that the two isothermal spheres model is indeed a speculation but it is presented as one of the possible solutions to remove the discrepancy. Subsequent papers will give a more detailed analysis of the cluster properties and mass models that we are studying based on our multi-frequency dataset. Throughout this paper, we assume $H_0 = 50$ h_{50} km s^{-1} Mpc^{-1}, the density parameter $\Omega = 1$, and the cosmological constant $\Lambda = 0$, unless otherwise stated. At the redshift of the cluster, the luminosity distance is 1231 h_{50}^{-1} Mpc, the angular size distance is 860 h_{50}^{-1} Mpc, and the scale is 4.17 h_{50}^{-1} kpc per arcsec.

2. HST Imaging

2.1. Observations and photometry

We acquired 10 exposures on consecutive orbits with the WFPC2 and the F702W filter in October 1994, for a total integration time of 22,200 s. The core of the cluster fits conveniently inside the $1.'3 \times 1.'3$ field of view of the Wide Field Camera 3 (WFC3), the best performing chip. The pixel size in this camera is 99.6 milliarcsec (Holtzman *et al.* 1995). Each exposure was offset by an integer number of pixels in both axes to aid in the correction for cosmic rays, dead pixels, and hot pixels. The standard STScI processed frames were registered and co-added using IRAF/STSDAS routines. The final 4-chip mosaic frame is shown in Figure 1 (Plate). The diffuse light, mostly from the envelope of the cD galaxy and partially from other galaxies, is detectable everywhere in the lensing region of this cluster. In Figure 2 (Plate), the diffuse light from the galaxies is diminished to bring out sharp structures by subtracting an image composed of the

median value in a 19 by 19 pixel box around each pixel.

The photometry was performed using the faint galaxy photometry software described in Le Fèvre *et al.* (1986), and Lilly *et al.* (1996). The photometric calibration was based on the HST calibration coefficients (Holtzman *et al.* 1995) and confirmed by our ground based imaging (Luppino *et al.* 1993) within 0.1 magnitude. Manual intervention was required to include the arcs with the largest axis ratio, which were not identified by the software. The histogram of number counts with Johnson R band magnitude is presented in Figure 3. The number counts decline for $R \geq 26$ indicating that the counts are incomplete at fainter magnitudes. A total of 901 objects with peak intensity above $\mu_R =25.5$ mag arcsec^{-2} (3σ over the sky background) have been identified in the 4.71 arcmin^2 HST field usable for photometry. Table 1 gives the R surface brightness in mag arcsec^{-2} for the objects with available spectroscopy (see Section 3. for a description and Figure 4). The peak of the light distribution has been determined after removal of the bright star next to the core. After a gaussian filter with $\sigma = 20$ pixels was applied to the image, the peak of the light distribution is measured to be $1''6$ from galaxy A. Ellipse fitting of the light envelope of the central core for the $\mu_R = 24.25$ mag arcsec^{-2} isophote indicates a major axis of $25''$, an ellipticity of $\epsilon = 0.17$, with $\epsilon = (a^2 - b^2)/(a^2 + b^2)$, and a position angle of $78°$. The center of this isophote fitting, indicated by a cross in Figure 2, is at $\alpha = 04^h 43^m 09^s.71$ and $\delta = +02°10'18''.66$ (J2000), just $1''2$ North and $1''1$ West from galaxy A.

2.2. Arcs and Arclets

The arc system is remarkable for the symmetry of the distortion pattern, and the large number of very elongated arcs. The most spectacular arc system is formed by arcs A2 and A3 (see Figure 2) which are resolved into bright knots by the HST. The very high axial ratios of these arcs indicate that they are quite near the critical radius. Arc A1, which was the most spectacular looking arc in the ground based image, appears to be a highly distorted image of a galaxy but not necessarily a strongly lensed object and we have found no other counter images of it. Arcs A5 and A6 both have multiple knots. Each of these knots, when reconstructed at the source plane, merges together with its counter image. The ability to bring these two intricate arcs together in a consistent way is a key requirement for a successful reconstruction for this cluster. Arcs A8 and A9 are very close to each other and are at nearly the same distance from the center of the light distribution. It is most probable that they emanate from a single object near the critical radius. The critical radius in the image plane grows with the redshift of the source, therefore the source of arcs A8 and A9 must be at a lower redshift than the source for arcs A2 and A3.

2.3. Radial Arcs

Two radial structures are observed near the center of the cluster. To identify the geometry of each feature more clearly and measure its magnitude, we have processed the central region of the cluster in the following manner. The two galaxies at the northern edge of the radial arc A17 have been modeled with $r^{1/4}$ profiles, and then subtracted from the image. A gaussian filter with $\sigma = 2$ pixels was then applied to the resulting image, and the result was subtracted from the non-filtered image. One arc is the slightly curved feature (A17 in Figure 2) $6''.5$ to the North of galaxy A. It subtends $2''.5$, and has a magnitude $R = 25.6 \pm 0.3$. Another radial feature is observed $4''$ North of galaxy B (A16 in Figure 2). It subtends $2''$ with $R = 27.2 \pm 0.6$ and is thus a more marginal feature. Both radial arcs have been used in the reconstruction to background source galaxies of this cluster.

3. Spectroscopic data

Spectroscopy was obtained in the field of MS0440+0204 in October 1993 with the Canada-France-Hawaii Telescope (CFHT) equipped with the Multi-Object Spectrograph (Le Fèvre *et al.* 1994). The O300 grism was used to provide a wavelength coverage from 4500 Å to 9000 Åand a pixel size of 5.5 Å/pixel. A slit width of $1''.5$ was used, providing a spectral resolution of 17 Å. Each 30 minute exposure was offset to allow removal of cosmic rays and bad pixels. The total exposure times for each object ranged from 2 to 3.5 hrs depending on which masks the object was seen through and on weather conditions (mean seeing $\sim 1''.5$). The data were reduced using the MULTIRED package developed by Le Fèvre *et al.* (1995). Fourteen galaxies, out of 15 objects observed, are cluster members. One galaxy is the arc-like structure to the East of the cluster core (A1 in Figure 2).

MS0440+0204 was also observed in November 1993, at the Multiple Mirror Telescope (MMT) with the Red Channel spectrograph and the 300 gr/mm grating. Exposures between 1 and 1.5 hrs were made using 7 aperture plates with between 7 and 10 slits each. The pixel size was 3.21 Å/pixel, the spectral resolution was 10 Å, and the seeing was between $1''$ and $1''.5$. Standard data reduction and velocity measurements with the XCSAO package under IRAF confirmed 37 cluster members. Nine cluster galaxies (labelled as G6, G10, G13, G18, G26, G28, G30, G33 and G35 in Figure 4) are in common with the CFHT observations, thus allowing an estimate of external errors. The average velocity difference from the common data is $< v_{(MMT)} - v_{(CFHT)} >=227$ km s^{-1} with an *rms* dispersion of 327 km s^{-1}.

We attempted to obtain long-slit spectroscopy of the brightest arcs in MS0440+0204 in January and October 1995 with the Low Resolution Imaging Spectrograph (LRIS) at the W. M. Keck 10m telescope. Poor weather and problems with the instrumentation prevented us from obtaining additional useful spectra of arcs. However, part of the data from both runs could be used to obtain spectra for 10 objects. These objects happened to fall in the $1'' \times 3'$ or $1''.5 \times 3'$ slits

that were positioned on the arcs. The 300 gr/mm grating was used which gives a pixel size of 2.5 Å/pixel. Four objects are cluster members (1 in common with MMT data; G8 in Figure 4), one object at $\sim 1\!\!'.6$ to the Southwest of the cluster is a QSO, another is an M star, and the remaining objects are galaxies in the background of the cluster. Their redshifts range from 0.387 to 0.777, but none of these galaxies lies within the effective strong-lensing area.

All the objects with spectroscopy are listed in Table 1 and marked in Figure 4. For each object the measured velocity (barycentric) plus its 1σ error, and redshift are given. Galaxies marked as G, C, and K in Figure 4 have been observed with the MMT, the CFHT, and the Keck telescope, respectively. K5 denotes the QSO in the field at z=0.4719±0.0006. Velocities are given for eight additional galaxies (marked 1 through 8) which are not cluster members (redshifts range from 0.0766 to 0.2617). Galaxy C4 is outside the field of view of Figure 4.

In total, 54 objects have securely identified redshifts in the field and 40 objects are consistent with being cluster members (marked with an asterisk in Table 1). The velocity histogram for the 44 galaxies with the approximate redshifts of MS0440+0204 is shown in Figure 5. There is a low-velocity extension in the histogram at 55,000 km s^{-1} (4 galaxies) that our 3σ clipping iterative algorithm (following Danese *et al.* 1980) excludes from the computation of the cluster velocity. From 40 accepted cluster members, we obtain a mean velocity of $<$v$> = 58,909$±142 km s^{-1} and a dispersion along the line of sight of $\sigma_{los} = 872^{+124}_{-90}$ km s^{-1}. Carlberg *et al.* 1996 found a value of 606±62 km s^{-1} for the velocity dispersion of MS0440+0204. They attribute their lower determination of velocity dispersion in a number of clusters to three factors (see their paper, section 3.3). Among them is the fact that the larger radial range covered by their data makes their data less vulnerable to the presence of local substructures which might affect the velocity dispersion.

Figure 5 includes a gaussian distribution centered at the redshift of the cluster, of the appropriate width, and with area normalized to the 40 cluster galaxies. From these data, the redshift of the cluster is measured to be 0.1965±0.0005.

The CFHT optical spectrum for galaxy A1 (see Figure 2 and Table 1) is shown in Figure 6. The presence of four emission lines in the spectrum unequivocally identifies this galaxy as a lensed background galaxy to the cluster at z=0.5317±0.0003.

4. X-ray data

4.1. ASCA temperature

MS0440+0204 was observed by ASCA (Tanaka, Inoue & Holt, 1994) in September 1994 for 40,000 s. The ASCA instrumentation consists of two Solid-State Imaging Spectrometers (SIS) sensitive in the range 0.5−9 keV (140 eV resolution at E=6 keV), and two Gas Imaging Spectrometers (GIS) with poorer energy resolution but with some efficiency up to 11 keV. The

SIS observations were performed in 4 CCD-Bright mode for Medium bit rate observations. Data preparation and analysis were done using the XSELECT and FTOOLS software packages which allow selection of valid time intervals and removal of hot and flickering pixels. Additional analysis was performed using the XSPEC package. For the spectral analysis we use the summed spectra of the two GIS and of SIS0. SIS1 spectrum was not used because of a contamination problem in the detector. The spatial resolution of ASCA along with the low signal-to-noise of the data permitted only a global single-temperature Raymond-Smith model (Raymond and Smith 1977) to be fitted to the data. The hydrogen column density was fixed to the Galactic value along the line of sight at the cluster position, $N_H = 9.12 \times 10^{20}$ cm^{-2} (Stark *et al.* 1992), and the heavy elements abundance was fixed to 0.3 of the solar value. This value was chosen since the typical range of measured abundances for clusters with temperatures between 2 and 6 keV lie between 0.3 and 0.4 solar (Ohashi 1996). The region containing the QSO could not be excluded from the analysis given its proximity to the cluster centre (1′.6, less than the half power diameter of the point spread function of the ASCA XRT +GIS, Makishima *et al.* 1996). A temperature of $kT = 5.5^{+0.8}_{-0.6}$ keV (90% confidence interval) was measured for the cluster gas. The inclusion of the QSO in the analysis would raise the fitted cluster temperature by only 6.5%. This variation is within the temperature errors and it is thus negligible for our purposes.

4.2. ROSAT imaging

X-ray observations of MS0440+0204 were obtained with the ROSAT High Resolution Imager (HRI, Trümper 1983) in two pointings in February 1994 and in August 1995, for a net live time of 27,015 s. The HRI operates in the ROSAT 0.1−2.4 keV energy band and provides an angular resolution of $\sim 4''$ (FWHM).

X-ray iso-intensity contours of MS0440+0204 are shown in Figure 7 overlaid on an optical CCD frame. We first created an X-ray image with a pixel size of $1''$ and then smoothed the image with a Gaussian of $\sigma = 4''$. The coordinates of the X-ray centroid are α(J2000) $= 04^h43^m09^s.8$ and δ(J2000) $= 02°10'19''.5$, corresponding to a position $2''$ North of galaxy A, and within $1''.5$ from the peak of the light distribution. The X-ray emission has average ellipticity $\epsilon = 0.15\pm0.02$. The position angle of the major axis with respect to the North axis (counterclockwise positive) is PA=120° for the innermost isophotes, and PA= 80° for the outer isophotes. The center of iso-intensity contours is consistent with the X-ray centroid thus confirming the symmetry of emission in the cluster. The bright point-like source seen in the contours in Figure 7 at $1'.6$ Southwest of the cluster center at $\alpha = 04^h43^m05^s.8$ and $\delta =+02°09'05''.5$ (J2000) is the QSO.

There are 768 ± 70 net counts in the cluster region within a circle of $140''$ radius (583 h$^{-1}_{50}$ kpc at the distance of the cluster) after subtraction of the emission due to the QSO. Assuming a temperature of 5.5 keV, as determined from ASCA data, fractional metallicity of 0.3 the solar value, and hydrogen column density along the line of sight N_H=9.12$\times10^{20}$ cm^{-2}, we determine a flux in the 0.1−2.4 keV energy band of $(1.57\pm0.14) \times 10^{-12}$ erg cm^{-2} s^{-1}. The X-ray luminosity

in the same energy band is $L_x=(2.85\pm0.25)\times10^{44}$ h_{50}^{-2} erg s^{-1}. The point-like source identified with the QSO has 136 ± 16 net counts in a $28''$ radius circle. Assuming a power law spectrum with an energy index $\alpha=1.0$ and the same N_H as before, the flux in the $0.1-2.4$ keV band is $(4.2\pm0.5)\times10^{-13}$ erg cm^{-2} s^{-1}. The corresponding QSO X-ray luminosity is $(4.8\pm0.6)\times10^{44}$ h_{50}^{-2} erg s^{-1}.

4.3. X-ray Profile

A radial profile of the X-ray emission is obtained by summing the HRI counts in concentric annuli of width $2''$ centered on the peak of the X-ray emission and dividing by the area of the annuli. This is possible out to a radius of $140''$ (583 h_{50}^{-1} kpc) at which point the profile becomes indistinguishable, within the noise, from the background level. The profile is then fit with a β model (Cavaliere and Fusco-Femiano, 1976) described by the standard form $S(r) = S_0(1 + r^2/r_c^2)^{-3\beta+1/2}$, with S_0 = central surface brightness, r_c = core radius and β = slope parameter. The values of the best fit are $S_0 = 2.2 \times10^{-12}$ erg cm^{-2} s^{-1} arcmin^{-2}, $r_c = 8''.0 \pm 1''.1$ and $\beta = 0.46 \pm 0.03$. Figure 8 shows this fit to be well within the errors. Using the HRI point spread function described in the Rosat User's Handbook, we deconvolved an azimuthally symmetric image generated by revolving the fit. A best fit of the β model to the profile of the deconvolved image has parameters $r_c = 6''.4 \pm 1''.1$ and $\beta = 0.45 \pm 0.03$. At the distance of the cluster this core radius corresponds to 26.7 h_{50}^{-1} kpc. The size of the core radius could indicate the presence of a cooling flow. However, there is no evidence for excess emission in the very core of the cluster, thus any cooling flow must be of marginal significance. Small core radii (less than 40–50 kpc) and small β values (~ 0.5), such as this cluster seems to have, have been observed recently in other clusters; see for instance MS1512+3647 ($r_c = 6''.9 \pm 1''.1$, $\beta = 0.524 \pm 0.031$; Hamana et $al.$ 1997) or our own unpublished HRI data for MS2137-2353. The small size of the core radii and βs for these X-ray selected clusters is an issue that will be investigated in future work.

5. Results

5.1. Light and gas distribution

The optical morphology of MS0440+0204 is unusual. It is a poor cluster with a luminous and compact core (R=14.8 within $24''$) characterized by the presence of several bright galaxies and numerous fainter ones, all embedded in the low surface brightness halo. As suggested earlier (Luppino et $al.$ 1993), we may be seeing a cD galaxy in the act of cannibalism. We have applied a gaussian filter with comparable σ ($2''$ in the HST image and $4''$ in the X-ray image) to compare the light and gas distribution of the cluster core. The X-ray centroid is within $1''.5$ from the peak of the light distribution: both distributions have almost circular symmetry with similar ellipticity values ($\epsilon = 0.17$ in optical vs. $\epsilon = 0.15$ in X-rays). We now proceed to determine the mass of the cluster from each of three techniques, and compare one with the other.

5.2. Mass estimate: Virial

An estimate of the cluster mass is first attempted using the optical data, via application of the virial theorem. From the virial theorem equation $M = 3R_v \sigma_{los}^2/G$ and using the measured $\sigma_{los} = 872$ km s^{-1}, a mass of $4.8^{+1.5}_{-0.94} \times 10^{14}$ h$^{-1}_{50} M_\odot$ is obtained for a value of the three-dimensional virial radius R$_v$=0.91 h$^{-1}_{50}$ Mpc (R$_v = (\pi/2)R_H$ where R$_H$ is the projected harmonic mean radius). This mass is defined by the radial extent of the region sampled; it is an underestimate of the total mass if the cluster extends beyond the size of the observed field (in our case ~ 1.5 h$^{-1}_{50}$ Mpc). We remind the reader that the accuracy of this method depends on the assumptions that the velocity dispersion is isotropic and that the cluster is no longer undergoing net expansion or contraction.

5.3. Mass estimate: X-ray

Although there is no concern about isotropy of the X-ray emitting gas, the mass determined using X-ray data does depend on assumptions involving spherical symmetry and hydrostatic equilibrium. These assumptions are found to be valid on the average in N-body simulations studies of cluster formation by Schindler *et al.* (1996) and Evrard *et al.* (1996). MS0440+0204 does not have any obvious substructure or strong shock wave that could affect the mass determination. The cluster seems a relatively undisturbed cluster (see Figure 7). The presence of small bumps may be caused by some motion of collisionless matter and of intracluster gas. Allen *et al.* (1996) caution against the use of single-phase analyses with ROSAT data, since the presence of a cooling flow with distributed mass deposition implies that the central Intra Cluster Medium (ICM) has a range of temperatures and densities at any particular radius: i.e. the ICM is multi-phase. There is no evidence of any significant cooling flow in MS0440+0204, thus we feel that the assumptions adopted for the deprojection outlined below are largely correct. In any case it is not possible to resolve this cluster with *ASCA*, or try to model the temperature as a function of distance from the center of the cluster since there are not enough photons for good limits. Thus in the following we will assume that no temperature gradient is present.

From the HRI surface brightness profile, assuming a constant temperature, we have derived the three-dimensional density distribution of the gas from the two-dimensional image by following the deprojection technique of Arnaud (1988). The data have been binned this time in annuli of variable step (see plus signs in Figure 9 and Figure 10) to have enough counts in each bin and thus reduce the statistical uncertainty of the derived parameters. The integrated mass in all forms can then be derived as a function of radius directly from the equation of the hydrostatic equilibrium

$$M(r) = -\frac{rkT_g}{G\mu m_p} \left[\frac{d\ln\rho_g}{d\ln r} + \frac{d\ln T_g}{d\ln r} \right], \tag{1}$$

where the symbols have the standard notation. The radial dependence of the gas density ρ_g is given by the ROSAT HRI observations. T_g is the intra-cluster temperature, μ is the mean molecular weight of the gas, and m_p is the proton mass. The constant intra-cluster gas temperature of 5.5

keV measured by ASCA is assumed. Our estimates for the gas and gravitational mass within 140″ (∼600 h_{50}^{-1} kpc at the cluster redshift) are $(3.1\pm0.25) \times 10^{13}$ $h_{50}^{5/2} M_\odot$ and $(1.3\pm0.2) \times 10^{14}$ $h_{50}^{-1} M_\odot$. The corresponding gas mass fraction, M_{gas}/M_{tot}=(23±0.03)% $h_{50}^{3/2}$, is typical of the inner regions of rich clusters (David *et al.* 1995) and consistent with that of low redshift clusters (White and Fabian 1995).

We have also deprojected the finely binned X-ray profile of Figure 8 assuming the standard β model. Our version of this analysis follows. The volume emissivity, ϵ_v, is found from a deprojection of the profile. For the standard functional form, the deprojection yields $\epsilon_v \propto (1 + r^2/r_c^2)^{-3\beta}$. The emissivity is proportional to the density squared times the cooling function. If we assume the gas is nearly isothermal, the density is $\rho_g = \rho_g(0)(1 + r^2/r_c^2)^{-3\beta/2}$. The gas density distribution is presented, in Figure 9, in units of protons cm^{-3}. However, the normalization is irrelevant to all that follows. For the purpose of assessing various sources of error, we continue the analysis of the fit to the raw data as well as the fit to the deconvolved data, but, in the end, quote results from the deconvolved data.

If one substitutes the β model law into Equation 1, and assumes constant temperature gas, or at least that the density falls off much more rapidly than the temperature, then one finds the following expression for the underlying mass as a function of radius:

$$M(r) = \frac{3\beta r_c \sigma_g^2}{G} \frac{s^3}{1 + s^2}, \tag{2}$$

where $\sigma_g = \sqrt{kT_g/\mu m_p}$ is the 1-d velocity dispersion of the gas, and $s \equiv r/r_c$. The β model mass distribution for MS0440+0204 is shown as the dashed line (fit to deconvolved data) and dotted line (fit to raw data) in Figure 10.

The density distribution of the β model is easily evaluated to be of the following form:

$$\rho^T = \frac{1}{4\pi r^2} \frac{dM(r)}{dr} = \frac{\rho^T(0)}{3} \frac{3 + s^2}{(1 + s^2)^2}, \tag{3}$$

where $\rho^T(0) = 9\beta\sigma_g^2/4\pi G r_c^2$. This profile resembles an isothermal mass distribution at small radii, deviates by a maximum of 1.81 at $11r_c$ and asymptotically approaches 1.5 times the isothermal distribution at large radii.

To compare to the gravitational lens results, one needs the projected cumulative mass profile. The surface mass in the β model is given by

$$\Sigma(R) = 2 \int_0^\infty \rho^T dz = \frac{\pi}{3}\rho^T(0)r_c \frac{2 + S^2}{(1 + S^2)^{3/2}}, \tag{4}$$

where z is the distance along the line-of-sight, $S = R/r_c$, and R refers to the radius in the plane of the sky. This, as it turns out, is exactly the same form as the surface density derived from the "isothermal" case ($\alpha = 1/2$) of the Blandford-Kochanek formula of the lensing potential (Blandford and Kochanek, 1987). The normalizations are also equal by setting $\sigma_{BK} = \sqrt{3\beta/2}\ \sigma_g$.

The projected cumulative mass profile is given by

$$M(R) = 2\pi \int \Sigma(R)RdR = \frac{2\pi^2}{3}\rho^T(0)r_c^3\sqrt{1+S^2}\left[1 - \frac{1}{1+S^2}\right],\tag{5}$$

and is shown as a dash-dot-dot-dot line in Figure 10. In the region of the observed multiple arc systems the projected mass is a few times the unprojected mass. At radii $>> r_c$, the projected mass eventually drops to $\pi/2$ times the unprojected mass at a similar radius.

We also examine an isothermal distribution for the underlying mass. A numerical solution to the differential equation of hydrostatic equilibrium is found for the case of constant temperature. A finely spaced solution of the density, $\rho_{iso}(s)$, is integrated to give $M(s)$ and $\int M(s)/s^2 ds$. The gas density distribution can be solved for in Equation 1:

$$\rho_g(r) = \rho_g(0)\exp\left[-\frac{G}{\sigma_g^2 r_c}\int_0^s \frac{M(s')}{s'^2}ds'\right].\tag{6}$$

We then square the gas density distribution, using the same core radius as in the β model, and project it onto the plane of the sky to compare with the observed deconvolved surface brightness.

Using the asymptotic solution at large radius for the isothermal sphere, an approximate value for the central density can be derived that matches the β model fit to the surface profile,

$$\rho_{iso}(0) = \frac{27\beta\sigma_g^2}{8\pi G r_c^2}\tag{7}$$

However, a better overall fit is found with $\rho_{iso}(0)$ at 0.77 times this value, as is shown in Figure 11. Even with some freedom in choosing r_c and ρ_0, the isothermal sphere model does not adequately fit at all radii. It appears that the simpler β model is, in fact, a better representation of the underlying mass distribution than an isothermal sphere.

5.4.   Mass limits: Lensing

A reconstruction of the arc images to background source galaxies was attempted using the morphological information in the HST images. As with other previously known lensing clusters (Kneib *et al.* 1996; Smail *et al.* 1997 among others) the high resolution of WFPC2 reveals significantly more lensed features than by using ground-based telescopes. Several arcs in MS0440+0204 are resolved by the HST into bright knots. Others like arc A1 which appeared as the most prominent arc from the ground data, is actually a distorted image of a galaxy but not necessarily a strong lensed object. We will follow and extend the nomenclature in Luppino *et al.* (1993) for both the galaxy names and the arcs. However, with the HST resolution available, we now think that objects labelled as A10, A14 and A15 are not strong arcs and they are not labelled

in Figure 2. Arc A11, which may be an arc, is out of the field of view of this image. A solution is obtained assuming a flattened potential (Blandford and Kochanek, 1987),

$$\phi = \frac{\pi\sigma_{BK}^2 r_c}{\alpha G}(1 + (1 - \epsilon)\text{x}^2 + (1 + \epsilon)\text{y}^2)^{-\alpha} \tag{8}$$

where r_c is the angular extent of the core radius, x is the run along the major axis in units of r_c, and y is the run along the minor axis. A position angle to align coordinates with the major axis must also be specified. The parameters σ_{BK}, r_c, and ϵ are simply fitting parameters and are not easily converted to any real physical quantities except in the $\alpha = 0.5$ case.

The observed position in the plane of the sky $X_{\alpha,\delta}^o$ is related to the source position $X_{\alpha,\delta}^s$ by,

$$\mathbf{X}_{\alpha,\delta}^o = \mathbf{X}_{\alpha,\delta}^s - \nabla_{x,y}\phi d_{ls}/d_s \tag{9}$$

where d_s is the comoving angular diameter distance of the source and d_{ls} is the comoving angular diameter distance of the source as seen by the lensing cluster (Hammer and Nottale, 1986; Peebles, 1993).

The full set of free parameters is: (x,y) position of center, position angle on the sky, r_c, α, ϵ, σ_{BK}, and the redshifts of all source objects. We do not restrict the model by the observed light distribution. In the end, the light and matter can be compared and information can be gleaned as to the degree to which the potential follows the light distribution.

The main difficulty stems from properly identifying which sets of arcs are to be associated as being counter images of the same source. The details of the model will be presented in Shaya *et al.* (1998). Here we present the results obtained for the mass determination. Since we do not have a redshift for any multi-arc system, we can obtain only upper limits to the mass and lower limits to the redshift. An upper limit to the mass derives from the fact that no credible counter image is found for Arc 1, the arc with known redshift. A lower limit ultimately derives from the fact that the term d_{ls}/d_s, in standard cosmologies with $\Omega = 1.0$ (0.1), approaches the finite value of 0.91 (0.84) as the redshift of the source goes to infinity.

Crude estimates for the values of the model parameters were first established by solving for the case that the pattern of 4 knots in A5 corresponds to the 4 knots in A6. With this model in hand one could explore different source plane distances to see what other arcs are counter images of each other. When another was found, a χ^2 minimization program to bring the knots of both systems together in the source plane provided more highly constrained values on the model parameters. This procedure was repeated, with more terms in the χ^2 each round, until no new set of counter images could be seen. If an incorrect association is made between arcs, then poor values for the parameters are assumed and this will lead to a dead end, in the sense that no new systems will be found. One must then back up and try a different pairing that will lead to further progress.

The following sets of arcs were found to be associated with their own source object with the range in redshifts set by the two limiting models: Arcs 5 and 6 (0.60 < z < 1.6), Arcs 8, 9, 12

and 24 (0.53 < z < 1.1), radial Arc 17 and Arc 18 (0.59 < z <1.5), Arc 7 and radial Arc 16 (0.59 < z < 1.5), and Arcs 2, 3, 20 and the faint, extreme Southern extension of A9 (0.75 < z < ∞). A best solution that solves for these arcs simultaneously requires values for $\epsilon = 0.074 \pm 0.005$, and for $r_c = 1''55 \pm 0.01$ corresponding to 6.4 h_{50}^{-1} kpc, a position angle of $74°2 \pm 1°4$, and $\alpha = 0.760 \pm 0.007$. However, these are uncorrelated errors. For correlated errors in which all of the other parameters are permitted to change as each parameter is tested, the errors in position angle and ellipticity are $2°4$ and 0.03, respectively. The core radius could be varied from 0 to $3''35$ (within 1 σ in χ^2). The value for α could be varied between 0.74 and 0.97 with little penalty in χ^2 except at the edges of this range.

The ellipticity in the lensing model reflects the ellipticity of the potential. It is expected to be about one third of the ellipticity of the underlying mass distribution (Mellier *et al.* 1993). Here, we find a ratio between the light distribution and the potential ellipticities of 2:1. It appears, therefore, that the value of the ellipticity of the light distribution is intermediate between that of the potential and the mass.

Arcs 5 and 6 identified in Figure 2 provide an important constraint on the mass geometry because a single source, with consistent complex structure, explains both. We failed to associate Arc 1, the only arc with known redshift at z=0.5317, with any counter image. If this is, indeed, because there is only one image, it provides an upper limit to the mass. For the maximal mass model, Arc 1 is allowed to be just beginning to form a counter image. At this point, the source image of Arc 1 is becoming alarmingly distended in a direction pointing toward the center. Thus a potential greater than the maximal mass model is unlikely, based solely on the form of the source image of Arc 1.

6. Discussion

The projected mass as a function of radius for X-ray data and lens modelling is presented in Figure 12. Out to the radius of 40 kpc, the X-ray mass model has just barely enough mass to be consistent with the lens mass. By 100 kpc, the outermost radius with strong lensing, the X-ray mass model appears to fall about a factor of 1.5 to 2 too low. The errors in the X-ray determined mass, are $\sim 24\%$ (90% confidence) after folding in errors in ASCA determined temperature with uncertainty in individual bin counts. Therefore, perhaps our model is too simple. The model that we describe below is presented as a possible way to reconcile the X-ray and lensing mass. Just adding a little more complexity to the model, and one that is well motivated by the complex structures observed on large scales, the X-ray and lens mass determinations can be reconciled. There may be other similarly complex models that resolve the mass discrepancy. Here we prove only the existence of a solution, not uniqueness.

It needs to be noted that the path followed by light from background sources is affected by the mass of the entire column through the line of sight. It may be that the projection of just

the cluster does not fully represent the total mass in the column. As a next simplest model, we look for a mass distribution made up of two isothermal spheres centered on the cluster which distributes the hot gas in such a way so that its surface brightness remains consistent with the observed X-ray brightness profile, but has a projected mass consistent with the gravitational lens results. It is true that we are extrapolating beyond the last point at which the gas could have been heated sufficiently to radiate X-rays. We are trying to reconcile here the disparity between X-ray determined mass and gravitational lens mass plus we are trying to understand the steep slope of the gravitational lens mass. Both problems are best dealt with by the proposed theory that clusters are embedded in superclusters. It is exactly the lack of information in the X-ray gas at large radii which we are exploiting to find a single model that fits both the X-ray and the gravitational lens. A solution is found with one isothermal sphere of core radius unchanged from the previous analysis but with a second sphere with core radius between $30 - 50$ times larger. For definiteness, we show a solution with 40 times larger core radius, $r_c = 1.06$ Mpc. The second component sphere has a central density 150 times less than the first component. The velocity dispersion of the second component is then $40/\sqrt{150} = 3.26$ times that of the first component, which put it at nearly $\sigma_v = 2000$ km s^{-1}. It is unclear, however, whether this component should be attributed to a second, warmer dark matter particle, or (more likely) to late fall into the cluster. Figure 13 compares the new density distribution (dash-dots) with the two from the previous sections, the β model (dotted) and the single isothermal sphere (dashed). The mass enclosed at each radius is presented in Figure 14. Although we continue the distribution out to 10 Mpc where it reaches a total mass of $2 \times 10^{16} M_\odot$, the distribution could start falling off at a few Mpc with little effect in what follows. The hump in the density and mass distributions beginning at a few 100 kpc could simply be a representation of the supercluster within which the cluster resides. In fact the total mass within 10 Mpc is quite reasonable for a major supercluster such as the Coma Supercluster or the Great Attractor.

We again use Equation 6 to calculate the expected X-ray profile and to set the normalization of ρ^T. This time the fit (Figure 15) fits well over most of the range but, admittedly, is a little low at 300 kpc, but it is nonetheless acceptable. The signal-to-noise is low at these radii and many of the bins give only upper limits. A slight error in background subtraction may contribute to the small discrepancies. Finally, the dash-dot line in Figure 12 shows the projection of the 2-isothermal spheres model and it appears to just fit the minimum mass model both in terms of slope and amplitude. The explanation then for the discrepancy between the X-ray determined mass and the gravitational lens mass might simply be the fact that the X-ray mass is not sensitive to the larger scale structure within which the cluster is embedded. We have not yet explored how sensitive the results are to coalignment of these two potentials. In future work, we will examine how stringent is the requirement for the cluster to be at the center of the larger scale structure.

Other alternatives for the cause of discrepancy include the possibility of temperature variations in the X-ray gas. We will have to wait for better X-ray spectroscopy with $AXAF$ since $ASCA$ cannot resolve this cluster. Bartelmann and Steinmetz (1996) suggested that the presence

of substructure and line-of-sight alignments of material towards the cluster core may contribute to the discrepancy observed, since they will increase the probability of detecting gravitational arcs in the clusters and thus enhance the lensing masses, without significantly affecting the X-ray data. The mass model prediction presented here will be tested by the weak lensing modelling which is underway by members of our team. The details may disagree because the supercluster is not expected to be spherically symmetric. The strong lens model examined in this paper is sensitive to the distribution along the line of sight to the center while the weak lensing will examine the distribution at large distances in the other two dimensions.

7.   Conclusions

The observational data from a multiwavelength study of the cluster MS0440+0204 have been presented, together with the analysis of the mass distribution as obtained by several techniques. For the HST/WFPC2 image, we focused on modelling of the gravitational lensed arcs distributed in the inner $24''$ radius. Ground based telescopes were used to obtain the velocity dispersion of the galaxies in the cluster and determine the virial mass. We used $ASCA$ data to derive a temperature for the X-ray gas. A $ROSAT/HRI$ image was used to derive an emission profile which is analyzed, assuming that the hot gas is in hydrostatic equilibrium and in a spherical potential, to derive the form of the cluster potential.

From possible multiple images formed by gravitational lensing of 5 background sources, we have derived limits to the mass distribution in the range $50 - 100$ h_{50}^{-1} kpc in MS0440+0204. For the central $24''$ (100 h_{50}^{-1} kpc) region encircled by the arcs, the possible range in projected mass is $6.6 - 9.5 \times 10^{13}$ $h_{50}^{-1} M_\odot$. The mass profile appears to grow with radius considerably more rapidly than an isothermal model or a β model. We have also used X-ray data to obtain a mass distribution from the inner few kpc out to nearly 600 h_{50}^{-1} kpc. There is no evidence for excess emission in the very core of the cluster which could indicate the existence of a cooling flow, thus justifying the assumption of constant temperature for the deprojection technique. The mass distribution obtained is well fit by a β model, described here, but not well fit by a single isothermal distribution. The X-ray derived projected mass profile is below the lensing mass profile. At 50 h_{50}^{-1} kpc, it is 20% below, which is just within the errors, but by 100 h_{50}^{-1} kpc it is a factor of 2 below. However, more general models fit the data better and allow a wider range of masses that are consistent with the lensing data.

The virial mass derived from the galaxy velocity dispersion, $4.8^{+1.5}_{-0.94} \times 10^{14}$ $h_{50}^{-1} M_\odot$ is intermediate between the extrapolations to 900 h_{50}^{-1} kpc of the other two profiles. As in other cases reported in the literature we find discrepancy between the X-ray and lensing estimates.

We tentatively explore the possibility of reconciling these mass estimates with a mass profile that increases more rapidly than the X-ray β model at large radii. The model explored is one with two isothermal spheres; one has a core radius of 26.7 h_{50}^{-1} kpc and the other core radius is 1 h_{50}^{-1}

Mpc. The central densities for the two components have a ratio of 150:1. With these parameters, a fit to the X-ray profile is reasonable and the projected mass profile is consistent with the minimum mass model for the gravitationally lensed arcs. The total mass out to 10 Mpc required by this model is about 2×10^{16} $h_{50}^{-1} M_{\odot}$, which could indicate the existence of a supercluster of galaxies with a mass comparable to the Coma Supercluster or the Great Attractor. Other alternatives for the discrepancy of the mass estimates include: a temperature gradient in the X-ray gas that may conspire against the models used; or the lensing mass could be higher because of line of sight projection effects. The asymmetric velocity distribution of the galaxies and its low end extension could be an indication that the mass of the cluster is not spherically distributed.

Similarly to other investigators we have found a discrepancy between the X-ray and lensing mass determination (see among others Miralda-Escudé and Babul, 1995; Kneib *et al.* 1995 or the exhaustive list of references in Wu and Fang, 1996, 1997). Differently from other lensing clusters with X-ray data, MS0440+0204 does not give evidence of any ongoing merger which could severely disturb the intracluster gas (i.e. like A2218, Kneib *et al.* 1995; A370, Mellier *et al.* 1994) and thus explain the discrepancy. The simple model presented here could be tested by: 1) a much deeper X-ray map showing more details of the behavior of the surface brightness profile (it may provide evidence of a second, large scale component) but a much larger field of view than that given by HRI would be necessary; 2) detection of a temperature gradient, possible with higher resolution instruments as the ones which will be flown on AXAF; 3) weak lensing analysis to greater radii using the large CCD mosaic camera with 8100×8100 pixels (Metzger, Luppino and Miyazaki, 1995) which will obtain wide field images of clusters at relatively low redshift such as the one presented here.

REFERENCES

Allen, S.W., Fabian. A.C. and Kneib, J.P., 1996, MNRAS, 279, 615

Allen, S.W., 1997, astro-ph/9710217.

Arnaud K.A. 1988, in "Cooling flows in Clusters and Galaxies", Fabian, A.C. ed, Kluwer Academic Publ. Dordrecht, p. 31

Bartelmann, M., and Steinmetz, M., 1996, MNRAS, 283, 431

Blandford, R.D. and Kochanek, C.S. 1987, ApJ, 321, 658

Carlberg, R.G., Yee, H.K.C., Ellingson, E., Abraham, R., Gravel, P., Morris, S. and Pritchet, C.J., 1996, ApJ462, 32

Cavaliere, A. and Fusco-Femiano, R., 1976, A&A, 49, 137

Danese, L., De Zotti, G. and di Tullio, G., 1980, A&A, 82, 322

David, L.P., Jones, C. Forman, W. 1995, ApJ, 445, 578

Ensslin, T.A., Biermann, P.L., Kronberg P.P. and Wu, X.-P., 1997, ApJ, 477, 560

Evrard, A.E., Metzler, C.A. and Navarro, J.F. 1996, ApJ, 469, 494

Fort, B. and Mellier, Y, 1994, A&A Rev., 5, 239

Gioia, I.M., Maccacaro, T., Morris, S., Schild, R.E., Stocke, J.T., Wolter, A. and Henry, J.P. 1990, ApJS, 72, 567

Gioia, I.M. and Luppino, G.A. 1994, ApJ, 432, 49

Hammer, F. and Nottale, L., 1986, A&A, 167, 1

Hamana, T., Hattori, M., Ebeling, H., Henry, J.P., Futamase, T. and Y. Shioya, 1997, ApJ, 484, 574

Henry, P.J. and Briel, U.G., 1995, ApJ, 443, L9.

Henry, P.J. and Briel, U.G., 1996, ApJ, 472, 137

Holtzman, J.A., Burrows, C.J., Casertano, S., Hester, J.J., Trauger, J.T., Watson, A.M. and Worthey, G., 1995, PASP, 107, 1065

Kaiser, N, and Squires, G., 1993, ApJ, 404, 441

Kneib, J.P., Mellier, Y., Pelló, R., Miralda-Escudé, J., Le Borgne, J.-F., Böhringer, H. and Picat, J.-P., 1995, A&A, 1995, 303, 27 (A2218)

Kneib, J.P., Ellis, R.S., Smail, I., Couch, W.J. and Sharples, R.M., 1996, ApJ, 471, 643

Le Fèvre, O., Bijaoui, A., Mathez, G., Picat, J.-P. and Lelièvre, G., 1986, A&A, 154, 92

Le Fèvre, O., Crampton, D., Felenbok, P., Monnet, G., 1994, A&A, 282, 325

Le Fèvre, O., Crampton, D., Lilly, S.J., Hammer, F., Tresse, L., 1995, ApJ, 455, 60.

Lilly, S.J., Le Fèvre, O.,Crampton, D., Hammer, F., Tresse, L., 1996, ApJ, 455, 50

Loeb, A. and Mao, S., 1994, ApJ, 435, L109

Luppino, G.A., Annis, J., Gioia, I.M., Le Fèvre , O. and Hammer, F. 1993, ApJ, 416, 444

Makishima, K. et al., 1996, PASJ, 48, 171

Markevitch, M., 1996, ApJ, 465, L1

Markevitch, M., 1997, ApJ, 483, L17

Mellier, Y., Fort, B., and Kneib, J-P., 1993, ApJ, 407, 33

Mellier, Y., Fort, B., Bonnet, H. and Kneib, J-P., 1994, in "Cosmological Aspects of X-ray clusters of galaxies", NATO ASI series C 441, Waltraut Seitter eds.

Metzger, M.R., Luppino, G.A., Miyazaki, S., 1995, Bull. American Astron. Soc., 187, #73.05

Miralda-Escudé, J. and Babul, A., 1995, ApJ, 449, 18

Ohashi, T. et al. 1996, in "Röntgenstrahlung from the Universe", H.U. Zimmermann, J.E. Trümper and H. Yorke eds., MPE report 263, pag 605-606.

Peebles, P.J.E., 1993, in "Principles of Physical Cosmology", (Princeton University Press: Princeton) P. 336.

Pierre, M. Le Borgne, J.F., Soucail, G. and Kneib, J.P., 1996, A&A, 311, 413

Raymond, J.C. and Smith, B.W., 1977 ApJS, 35, 419

Schindler, S. 1996, A&A, 756, 305

Shaya, E. et al., in preparation

Smail, I., Hogg, D.W., Blanford, R., Cohen, J.G., Edge, A.C., and Djorgovski, S.G., 1995a, MNRAS, 277, 1 (A2219)

Smail, I., Ellis, R.S., Fitchett, M.J., and Edge, A.C., 1995b, MNRAS, 273, 277 (MS1455 and MS0016)

Smail, I., Ellis, R.S., Dressler, A., Couch, W.J., Oemler, A., Sharples, R.M., and Butcher, H., 1997, ApJ, 479, 70

Squires, G., Kaiser, N., Babul, A., Fahlam, G., Woods, D., Neumann, D.M., Böhringer, H., 1996a, ApJ, 461, 572 (A2218)

Squires, G., Kaiser, N., Fahlam, G., Babul, A., Woods, D., 1996b, ApJ, 469, 73 (A2390)

Squires, G., Neumann, D.M., Kaiser, N., Arnaud, M., Babul, A., Böhringer, H., Fahlam and Woods, D., 1997, ApJ, 482, 648 (A2163)

Stark, A.A., Gammie, C.F., Wilson, R.W., Bally, J., Linke, R.A., 1992, ApJS, 79, 77

Tanaka, Y., Inoue, H., and Holt, S.S. 1994, PASJ, 46, L37

Trümper, J., 1983, Adv. Space. Res. 2, 142

Tyson, J.A., Valdes, F. and Wenk, R., 1990, ApJ, 349, L1

White, D.A. and Fabian, A.C., 1995, MNRAS, 273, 72

Wu, X.-P. and Fang, L.Z., 1996, ApJ, 467, L45

Wu, X.-P. and Fang, L.Z., 1997, ApJ, 483, 62

Fig. 1.— The full WFPC2 image of MS0440+0204 ($z = 0.1965$) in the F702W filter, sum of all exposures and cosmic ray cleaned. Orientation is explained in Figure 2.

Fig. 2.— WFC3 image, with local median average subtracted, of the central $51\rlap{.}''2 \times 51\rlap{.}''2$ (512 by 512 pixels) of MS0440+0204 with names given for each arc. The plus sign marks the center of mass. The cross sign indicates the center of this isophote fitting. The figure has to be rotated by 152.46 clockwise to have North up and East to the left.
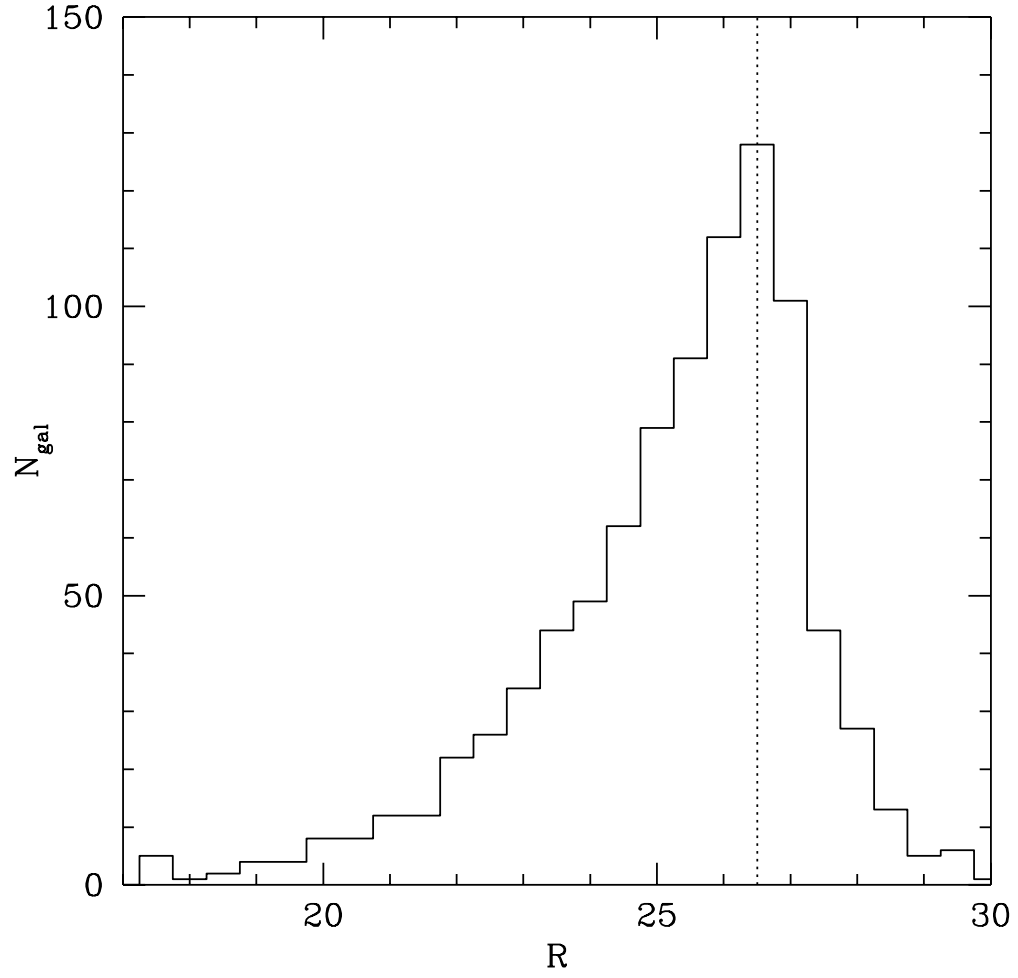
Fig. 3.— The R band magnitude number counts. The decline at $R \geq 26$ indicates that the counts are incomplete at fainter magnitudes.

Fig. 4.— B+R CCD image of MS0440+0204 (adapted from Gioia and Luppino, 1994) showing objects with spectroscopic data. The field of view is $3'.5 \times 3'.5$, corresponding to 0.87 Mpc $\times$ 0.87 Mpc at the redshift of the cluster (North is up and East to the left).
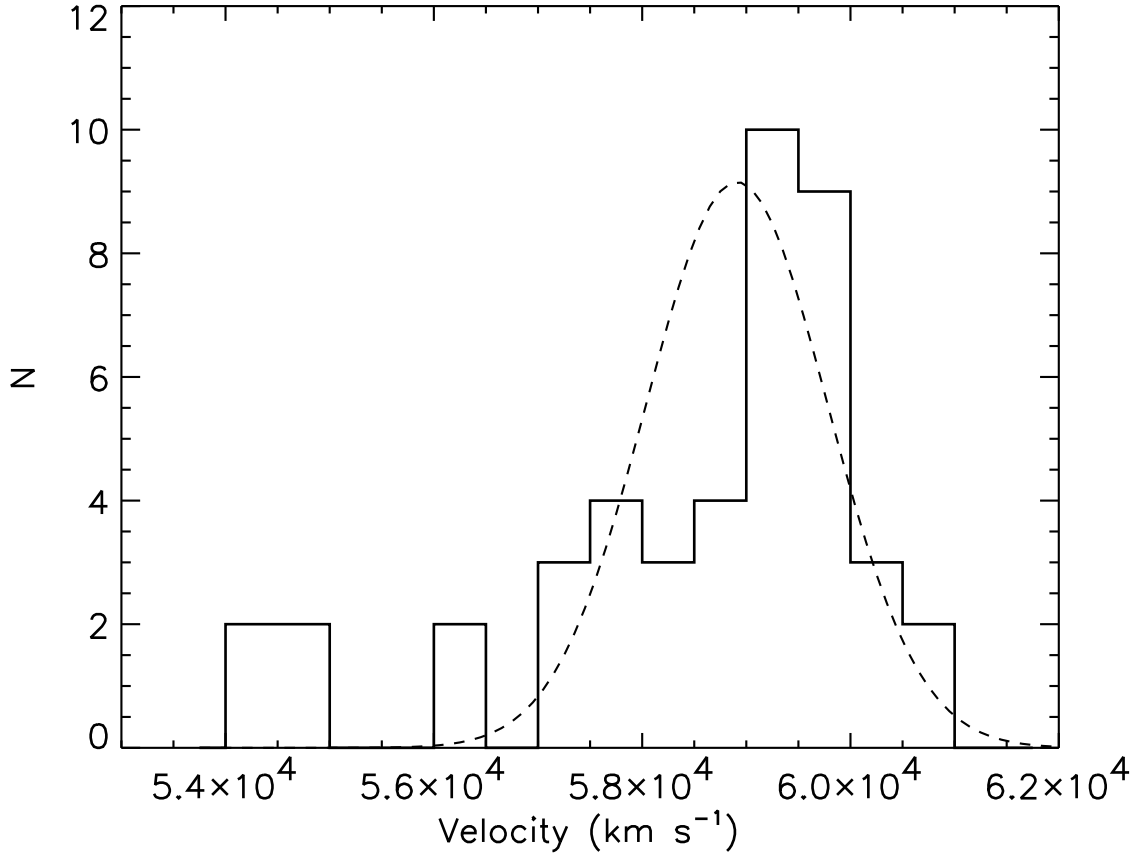
Fig. 5.— Distribution of velocities for the entire sample of 44 galaxies showing a low-velocity tail at 55,000 km s^{-1}. The curve shows a gaussian distribution with width given by the derived σ_v and normalized for the 40 galaxies considered cluster members.
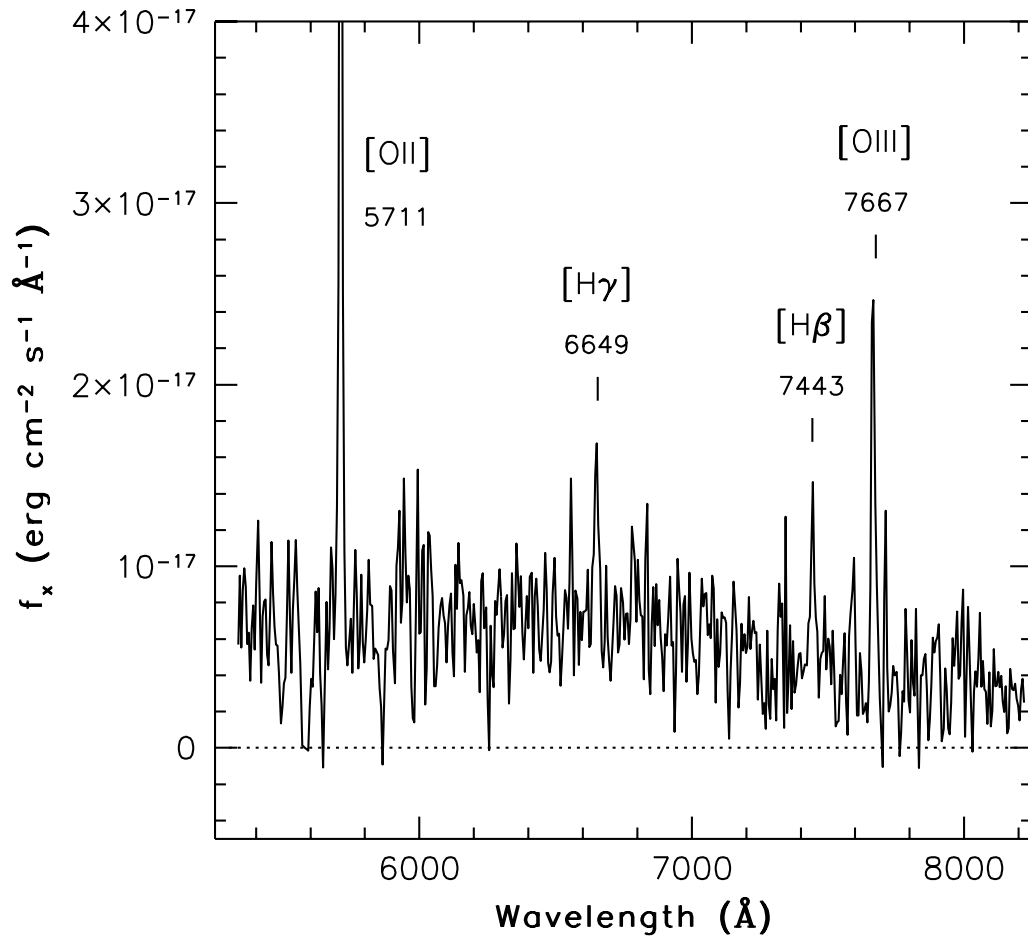
Fig. 6.— CFHT optical spectrum of the distorted arc-like galaxy A1 to the East of the cluster core. From O[II], Hγ, O[III] and Hβ emission lines a redshift of 0.5317 is obtained.

Fig. 7.— The HRI iso-intensity contour map overlaid on the optical CCD frame of Figure 6. The X-ray image is smoothed with a Gaussian with $\sigma = 4''$. Isophotal contours are 0.044, 0.062, 0.086, 0.115, 0.156, 0.231, and 0.306 net counts arcsec^{-2}, with the lowest contour being 40% above the background of 0.10957×10^{-5} counts arcsec^{-1}. The point-like source $1\rlap{.}'6$ to the Southwest is the QSO.
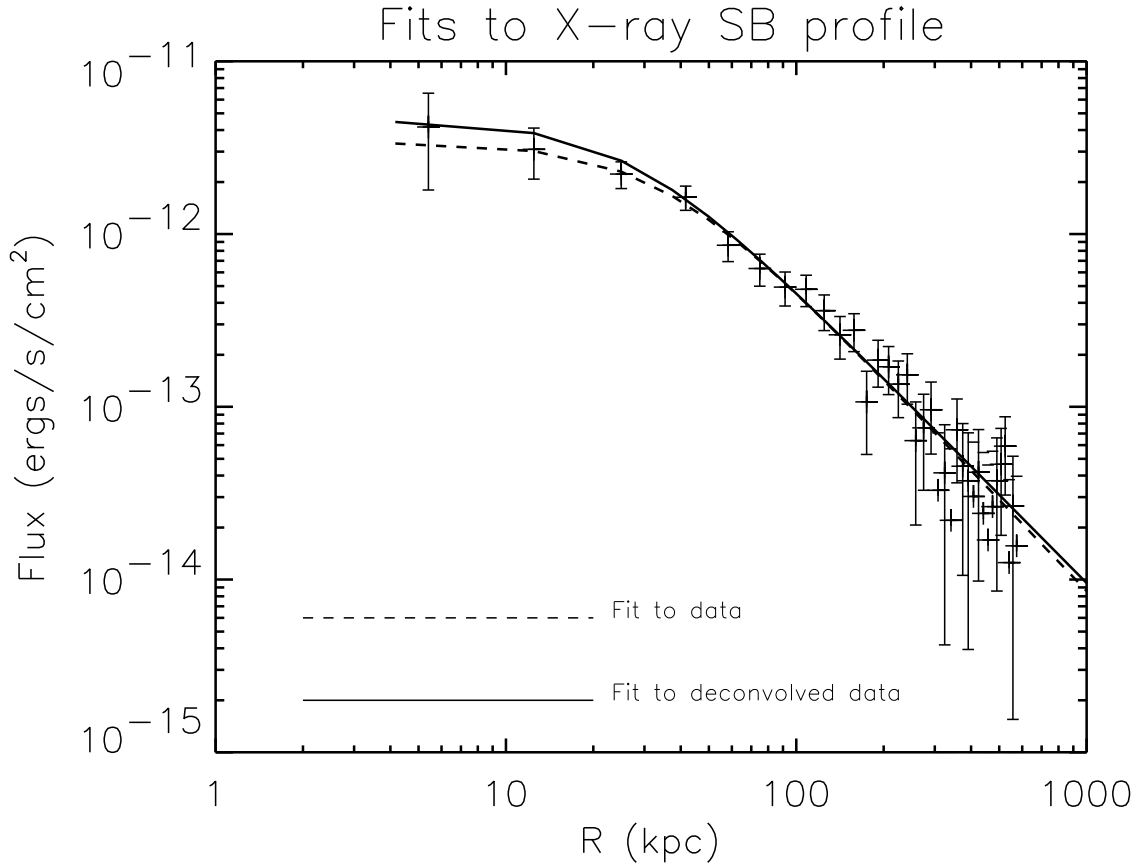
Fits to X-ray SB profile

Fig. 8.— The HRI brightness profile azimuthally averaged is presented as plus signs with error bars. The dashed line is the best fit of form $S(r) = S_0(1 + r^2/r_c^2)^{-3\beta+1/2}$. The solid line is the best fit of the same form to the deconvolution of the raw fit with the HRI point spread function. See text for values of fit parameters.
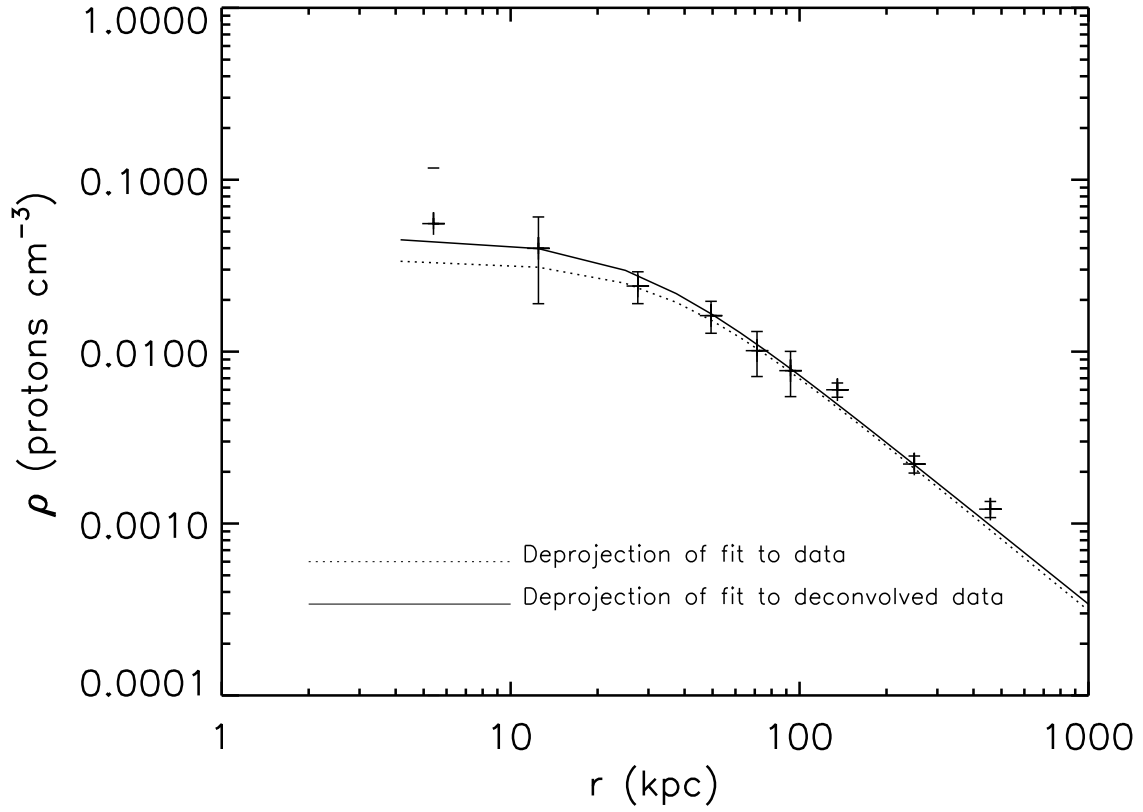
Fig. 9.— Gas density profile derived from HRI brightness profile. Plus signs are derived from coarsely binned data. See text for details. Dotted line is β model fit, $\rho_g = \rho_g(0)(1 + r^2/r_c^2)^{-3\beta/2}$ to the raw data. Solid line is the same but for the deconvolved data.

Fig. 10.— Cumulative mass with radius as derived from HRI brightness profile. Plus signs with error bars are found by coarsely binning the data and solving for M(r) independently for each bin. The dotted line is a β model fit to raw data. The dashed line is a β model fit to deconvolved data. The solid line is from a model in which the total mass is distributed as an isothermal sphere model. The thin lined error bar at 900 h_{50}^{-1} kpc shows the virial determination of the mass. The dash-dot-dot-dot line is the projection of the β model for comparison with gravitational lens mass determination. A vertical line is placed at the core radius of the fit.
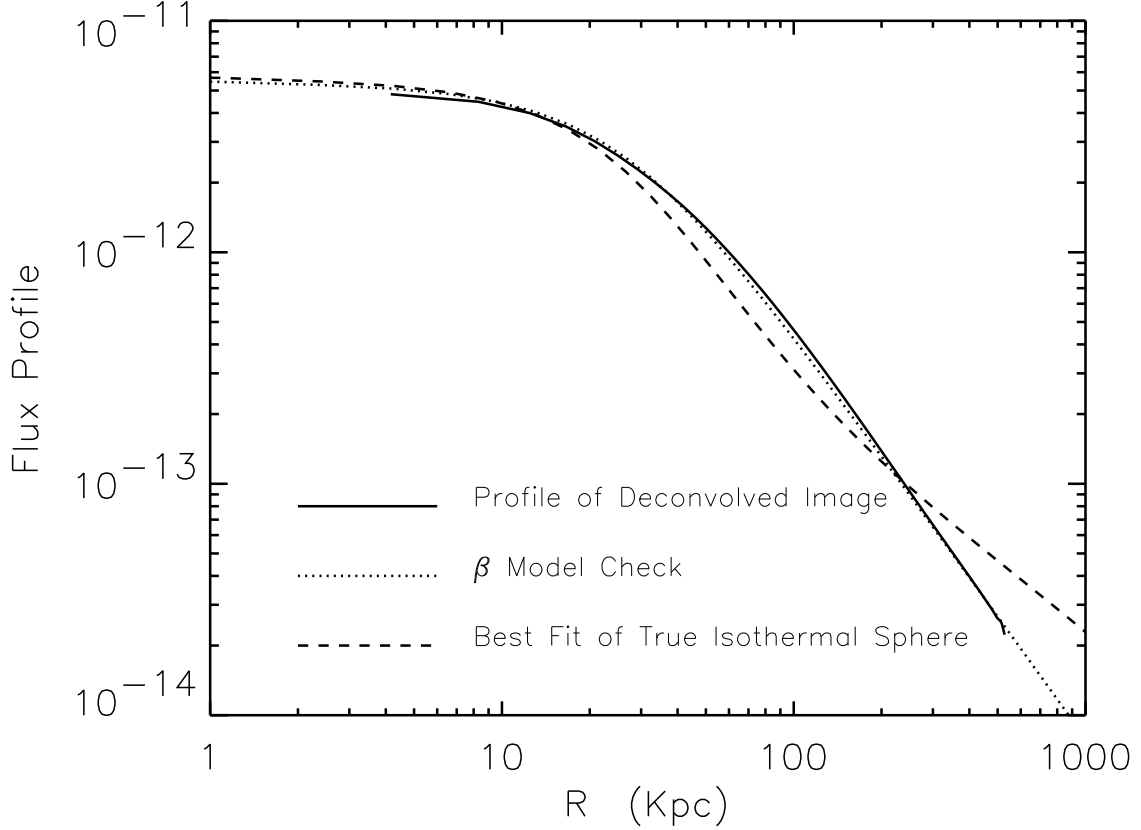
Fig. 11.— Calculations of the brightness profile given the total mass density distributions. See text for details. For the β model (dotted line), this amounts to reversing the procedure of deriving M(r) and is thus just a check of the total procedure. For the model with the total mass following an isothermal distribution (dashed line), the best normalization is determined by changing ρ^T and r_c iteratively until a good fit to the X-ray brightness profile is found. The β model is a significantly better fit.

Fig. 12.— Projected mass profile from lensing and X-ray data. The dash-dot-dot-dot line is the β model deprojection of the X-ray mass profile. From the gravitational lensing, the two solid lines represent the projected minimum and maximum mass models with $\alpha = 0.76$. The minimum acceptable value for α is 0.74. The dashed curve is from the model with the maximum acceptable value for $\alpha = 0.97$. The dash-dotted line is the projected mass of 2 isothermal spheres having $r_c = 26.7$ h_{50}^{-1} kpc and 1 h_{50}^{-1} Mpc and with ρ^T ratio of 1:150.
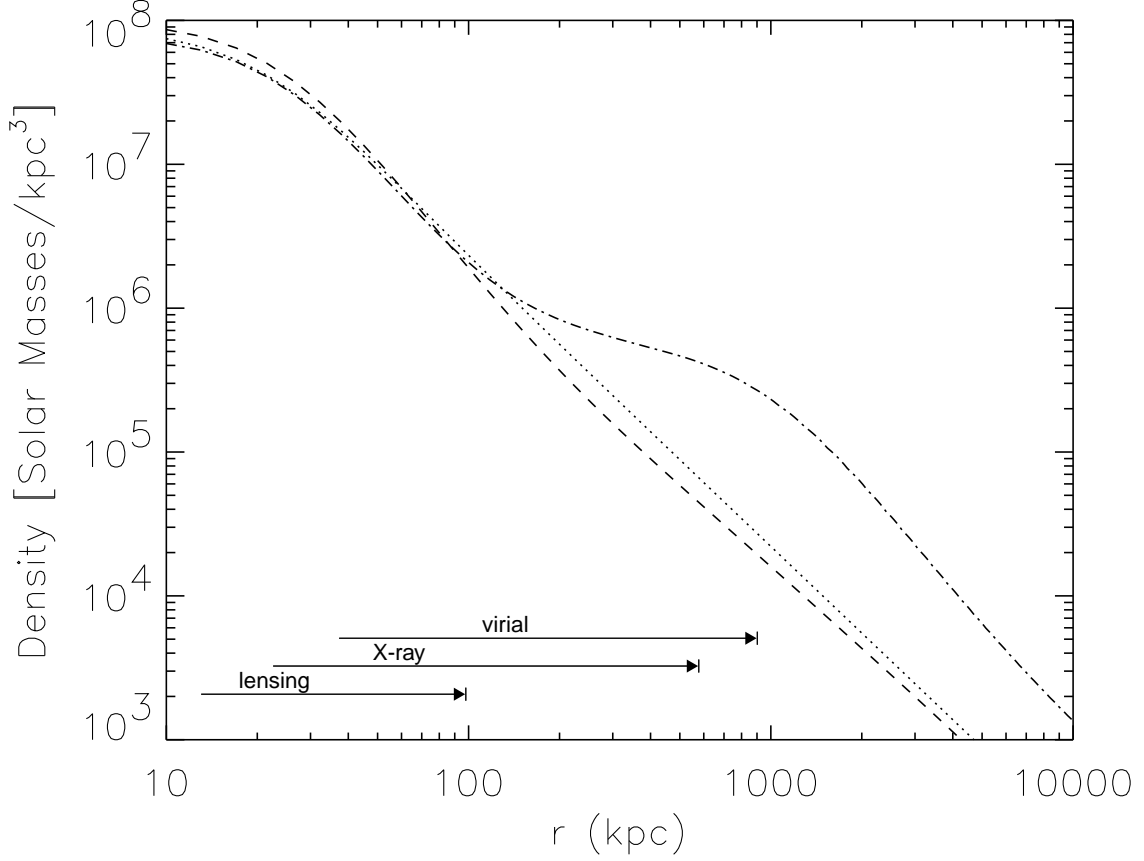
Fig. 13.— Density Distributions. 2 concentric isothermal mass spheres with $r_c = 26.7$ h_{50}^{-1} kpc and 1 h_{50}^{-1} Mpc, central density ratios 150:1 (dash-dotted line). Also shown are the single isothermal mass (dashed line) and the single β model (dotted line) used in the previous figures. The three thin solid lines parallel to the x-axis indicate the ranges in radius constrained by the different kinds of data.

Fig. 14.— Mass Distributions. 2 concentric isothermal mass spheres with $r_c = 26.7$ h_{50}^{-1} kpc and 1 h_{50}^{-1} Mpc, central density ratios 150:1 (dash-dotted line). Also shown are the single isothermal mass (dashed line) and the single β model (dotted line) used in the previous figures. The three thin solid lines parallel to the x-axis indicate the ranges in radius constrained by the different kinds of data.
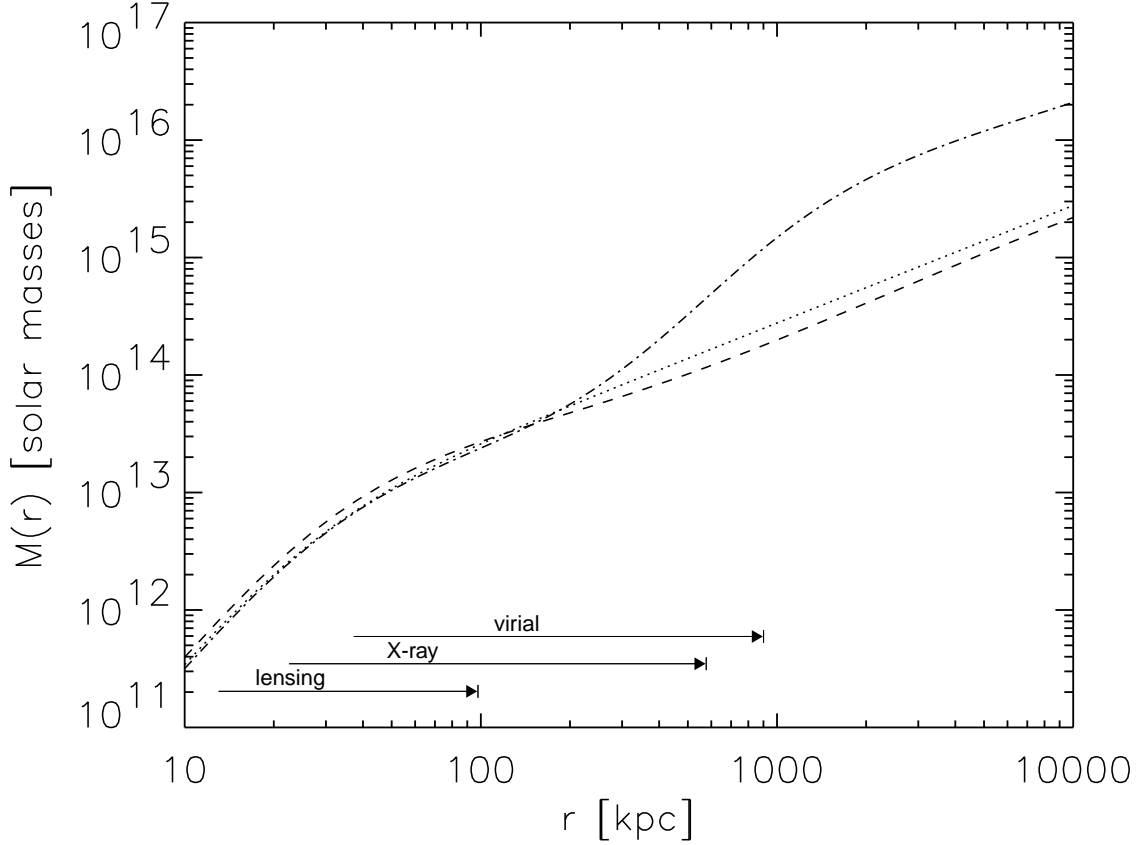
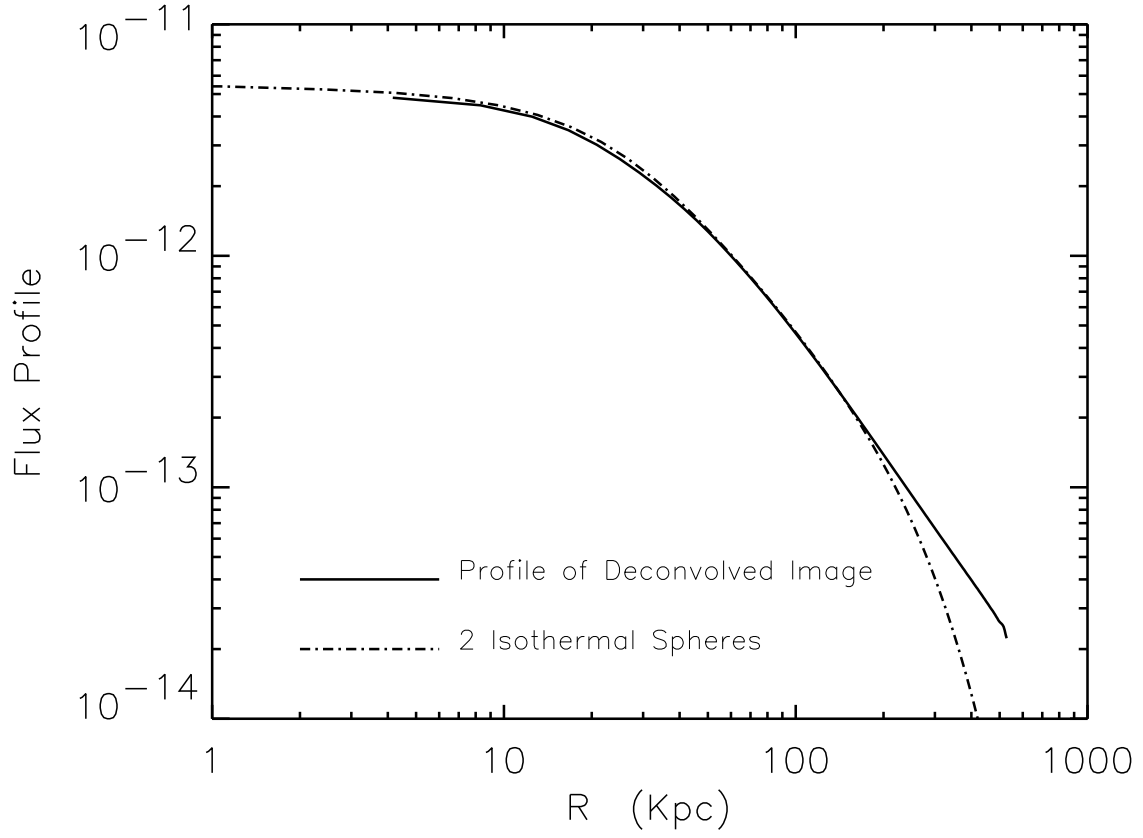Fig. 15.— X-ray Brightness profile. 2 concentric isothermal mass spheres with $r_c = 26.7$ h_{50}^{-1} kpc and 1 h_{50}^{-1} Mpc, central density ratios 150:1 (dash-dotted line). The solid line is the earlier β model fit to deconvolved data.

Table 1.   Photometric and spectroscopic data for the MS0440+0204 field.

Flag	R $mag/arcsec^2$	cz km/s	cz err	z
*G1		57414	62	0.1915
*G2	19.34	58551	160	0.1953
*G3	18.52	59563	39	0.1987
*G4	20.87	58953	153	0.1966
*G5	19.28	58437	91	0.1949
*G6		57188	74	0.1908
*G7		59070	200	0.1970
*G8	18.41	59772	43	0.1994
*G9	18.72	56352	41	0.1880
*G10		59525	65	0.1985
*G11		60655	90	0.2023
G12	19.96	54799	100	0.1828
*G13	17.70	56486	50	0.1884
*G14	19.58	59291	91	0.1978
*G15		60058	103	0.2003
G16	18.32	54426	52	0.1815
*G17	18.36	59036	79	0.1969
*G18		58780	61	0.1961
*G19		59098	70	0.1971
*G20		60193	203	0.2008
*G21		59831	84	0.1996
G22	20.25	54094	128	0.1804
*G23	20.12	60051	105	0.2003
*G24		57274	95	0.1910
*G25		59834	133	0.1996
*G26		57565	93	0.1920
G27		54998	176	0.1834
*G28		59459	82	0.1983
*G29	20.82	58366	81	0.1947
*G30	18.21	57797	53	0.1928
*G31		59256	175	0.1977
*G32	20.28	60908	79	0.2032
*G33	17.36	59539	103	0.1986
*G34		57655	84	0.1923
*G35	19.25	59557	90	0.1987
*G36		59229	103	0.1976
*G37	18.21	59169	69	0.1974
A1		159404	89	0.5317
*C1		57532	290	0.1929
*C2		59031	290	0.1969
*C3		59960		0.20
*C4		58221	290	0.1942
*K1	20.26	58821	89	0.1962
*K2	19.33	59510	119	0.1985
*K3	19.38	59091	150	0.1971

Table 1—Continued

Flag	R $mag/arcsec^2$	cz km/s	cz err	z
K4	17.26	star		M
K5	17.21	141476	180	0.4719
K6		160303		0.5347
K7		115993	90	0.3869
K8		232915	30	0.7769
K9		149690	600	0.4993
1	20.21	78458	140	0.2617
2		34581	81	0.1153
3		28236	78	0.0942
4		27374	149	0.0913
5		51428	108	0.1715
6		22960	83	0.0766
7	21.90	42203	124	0.1408
8		42255	116	0.1409

This figure "fig01.jpeg" is available in "jpeg" format from:

http://arXiv.org/ps/astro-ph/9712004v1

This figure "fig02.jpeg" is available in "jpeg" format from:

http://arXiv.org/ps/astro-ph/9712004v1

This figure "fig04.jpeg" is available in "jpeg" format from:

http://arXiv.org/ps/astro-ph/9712004v1

This figure "fig07.jpeg" is available in "jpeg" format from:

http://arXiv.org/ps/astro-ph/9712004v1